ELSEVIER

Contents lists available at ScienceDirect

# Journal of Biomechanics

journal homepage: www.elsevier.com/locate/jbiomech www.JBiomech.com



# Fluid-structure coupled biotransport processes in aortic valve disease



Mohammadreza Soltany Sadrabadi <sup>a</sup>, Mohammadali Hedayat <sup>b</sup>, Iman Borazjani <sup>b</sup>, Amirhossein Arzani <sup>a,\*</sup>

- <sup>a</sup> Department of Mechanical Engineering, Northern Arizona University, Flagstaff, AZ, USA
- <sup>b</sup> J. Mike Walker '66 Department of Mechanical Engineering, Texas A&M University, College Station, TX, USA

#### ARTICLE INFO

## Article history:

Accepted 4 January 2021

Keywords:
Hemodynamics
FSI
Mass transport
Shear stress
Lagrangian coherent structures

#### ABSTRACT

Biological transport processes near the aortic valve play a crucial role in calcific aortic valve disease initiation and bioprosthetic aortic valve thrombosis. Hemodynamics coupled with the dynamics of the leaflets regulate these transport patterns. Herein, two-way coupled fluid-structure interaction (FSI) simulations of a 2D bicuspid aortic valve and a 3D mechanical heart valve were performed and coupled with various convective mass transport models that represent some of the transport processes in calcification and thrombosis. Namely, five different continuum transport models were developed to study biochemicals that originate from the blood and the leaflets, as well as residence-time and flow stagnation. Low-density lipoprotein (LDL) and platelet activation were studied for their role in calcification and thrombosis, respectively. Coherent structures were identified using vorticity and Lagrangian coherent structures (LCS) for the 2D and 3D models, respectively. A very close connection between vortex structures and biochemical concentration patterns was shown where different vortices controlled the concentration patterns depending on the transport mechanism. Additionally, the relationship between leaflet concentration and wall shear stress was revealed. Our work shows that blood flow physics and coherent structures regulate the flow-mediated biological processes that are involved in aortic valve calcification and thrombosis, and therefore could be used in the design process to optimize heart valve replacement durability.

© 2021 Elsevier Ltd. All rights reserved.

### 1. Introduction

Calcific aortic valve disease (CAVD) and aortic valve thrombosis are major forms of aortic valve disease, which lead to valve stiffening, impaired valve dynamics, and obstruction of the blood flow supplied from the heart to the systemic circulation. CAVD is a multi-stage process (Pawade et al., 2015). The initiation phase of the disease resembles the inflammatory processes in atherosclerosis where dysfunctional valvular endothelial cells become exposed to the infiltration of low-density lipoprotein (LDL), oxidized LDL, and monocytes. Subsequently, the valve leaflets house a cascade of biochemical reactions (Arzani et al., 2017b), which ultimately gives rise to an inflammatory environment (Buendía et al., 2015). The inflammatory environment together with biomechanical forces promotes valvular interstitial cell differentiation and calcium deposition (Chen and Simmons, 2011; Pawade et al., 2015; Arzani and Mofrad, 2017).

Thrombosis is a major problem associated with aortic valve replacements. Patients receiving mechanical heart valves require

E-mail address: amir.arzani@nau.edu (A. Arzani).

lifelong anti-coagulation therapy (Kulik et al., 2006) and recently it has been shown that 40% of patients receiving transcatheter aortic valve replacement (TAVR) develop leaflet thrombosis (Makkar et al., 2015; De Marchena et al., 2015). Thrombosis is a highly complex process involving the reaction of several biochemicals and cells, which results in thrombus (blood clot) formation (Leiderman and Fogelson, 2011; Cito et al., 2013). Virchow's triad (Lowe, 2003) describes the three main factors influencing thrombosis: hypercoagulation, endothelial cell dysfunction, and blood flow stagnation. Effective thrombosis requires prolonged flow stagnation and increased accumulation and concentration of thrombogenic biochemicals near an exposed surface.

Biological transport processes near the highly deforming aortic valve leaflets play an important role in calcification and thrombosis. Blood flow is responsible for delivering LDL and monocytes into the valve leaflets during calcification initiation and prolonged accumulation of thrombogenic matter such as platelets due to disturbed flow patterns lead to thrombosis. Calcification is more likely to occur on the aortic side of the valve (Weinberg et al., 2010; Yip and Simmons, 2011), which accompanies complex near-leaflet flow patterns (Ge and Sotiropoulos, 2010). Additionally, blood flow

<sup>\*</sup> Corresponding author.

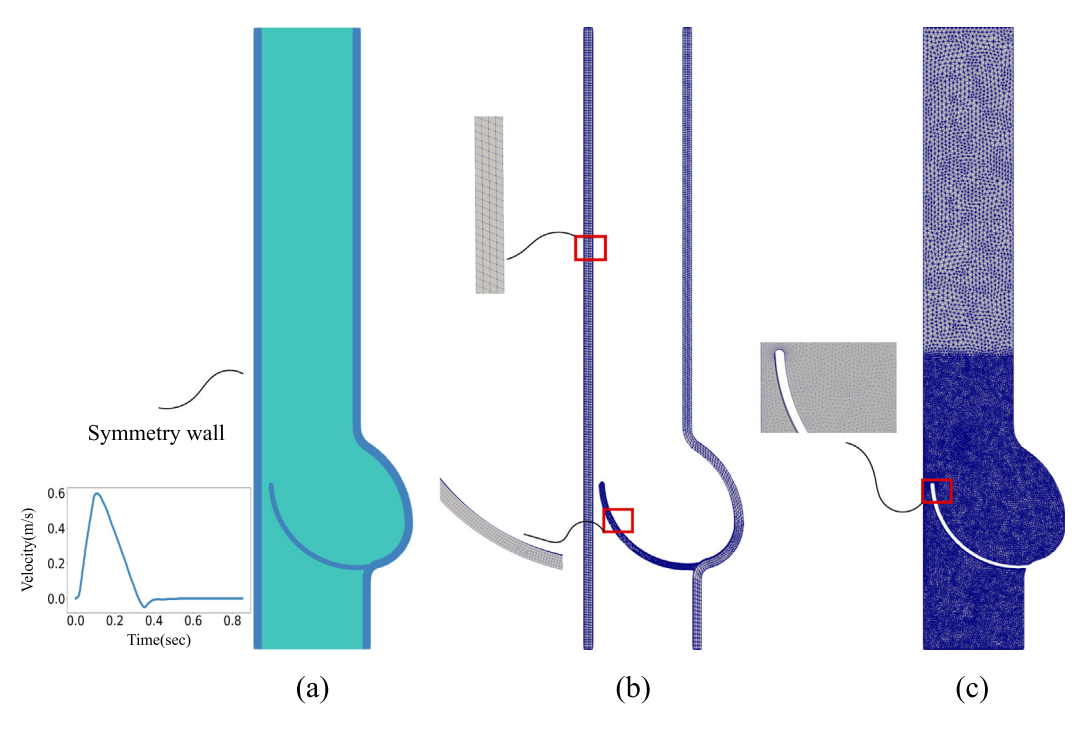


Fig. 1. a) The model geometry and inlet boundary condition, b) solid mesh, and c) fluid mesh are shown.

stagnation has been recently shown to be responsible for TAVR thrombosis (Midha et al., 2017; Raghav et al., 2019).

Computational modeling of aortic valve hemodynamics and transport is challenging. First, fluid-structure interaction (FSI) models need to deal with highly transient, nonlinear, and large deformations in a two-way coupled framework. Next, the FSI model needs to be coupled with a mass transport model, which represents its own numerical challenges due to the domination of advection (Hansen et al., 2019). In recent years, significant progress has been made in the FSI modeling of native (Weinberg and Mofrad, 2007; Cao and Sucosky, 2017; Gilmanov et al., 2019; Chen and Luo, 2020) and replaced aortic valves (Borazjani, 2013; Kamensky et al., 2015; Kandail et al., 2018; Ghosh et al., 2020). The majority of heart valve transport studies have focused on quantifying mechanical platelet activation potential using Lagrangian (Morbiducci et al., 2009; Xenos et al., 2010; Zakaria et al., 2017) and more recently Eulerian approaches (Hedayat et al., 2017; Hedayat and Borazjani, 2019). However, biotransport processes near aortic valve leaflets have received less attention. Recently, one-way coupled FSI has been used to study flow stagnation on valve leaflets (Vahidkhah and Azadani, 2017). However, a detailed analysis of different mass transport processes relevant to aortic valve calcification and thrombosis has not been reported.

The goal of this manuscript is to study the mass transport processes that influence aortic valve disease and understand their connection with the blood flow physics in a fluid–structure coupled environment. We hypothesize the vortex structures and their interaction with the valve leaflets control biotransport processes away and near the leaflet. We present different continuum transport models in a 2D model of a bicuspid aortic valve and extend our results to a 3D mechanical heart valve model.

#### 2. Methods

#### 2.1. Two-dimensional FSI model

Two-way coupled 2D FSI simulations were performed and coupled to continuum transport models using ANSYS 19.3. To enable

2D modeling in ANSYS, the model was slightly extruded in the dimension normal to the 2D plane. Different components of the FSI model are explained below.

**1- Structure:** A 2D idealized bicuspid aortic valve is assumed as the geometry. This model is a simplified model based on prior work (Weinberg and Mofrad, 2008). A symmetry plane is used to reduce the computational cost. The model contains the aortic valve leaflet, the aortic root, the sinus of Valsalva, and the ascending aorta as shown in Fig. 1. A contact condition is defined at the symmetry plane to simulate valve closure. The structural domain is divided into 68 k elements with a higher resolution around the leaflet (Fig. 1b). Linear elastic material with Young's modulus of 2 Mpa is prescribed for the wall. The nonlinear isotropic Ogden model is prescribed for the leaflet (Eq. 1):

$$W = \frac{\mu}{\alpha} (\lambda_1^{\alpha} + \lambda_2^{\alpha} + \lambda_3^{\alpha} - 3) + \frac{1}{2} K(J - 1)^2, \tag{1}$$

where  $\lambda_1,\lambda_2$ , and  $\lambda_3$  are principal stretches in the three directions,  $\mu$ , and  $\alpha$  are model constants, K is the bulk modulus, and  $J=\lambda_1\lambda_2\lambda_3\approx 1$ . The constants  $\alpha=12.275$  and  $\mu=75310$  Pa are obtained by fitting the stress–strain curve collected from experimental tests in (Korossis et al., 2002).

- **2- Fluid:** The fluid domain is simulated in Fluent. Blood is approximated as an incompressible and Newtonian fluid (density =  $1050 \text{kg/m}^3$ ; dynamic viscosity = 0.0035 Pa.s). The fluid domain is discretized into 435 k elements. The simulation timestep divided each cardiac cycle into 1500 time-steps. The velocity waveform profile from a prior study (Joda et al., 2019) (shown in Fig. 1) is used as the inlet boundary condition. Zero traction has been assumed for the outlet.
- **3- Coupled system:** The arbitrary Lagrangian–Eulerian (ALE) method is used for the FSI coupling system. Using the systems coupling module in ANSYS, displacement data is transferred from solid to fluid domain and traction is transferred from fluid to solid domain. Mesh smoothing and remeshing are used to overcome distorted elements, which are inevitable in large-deformation ALE simulations.

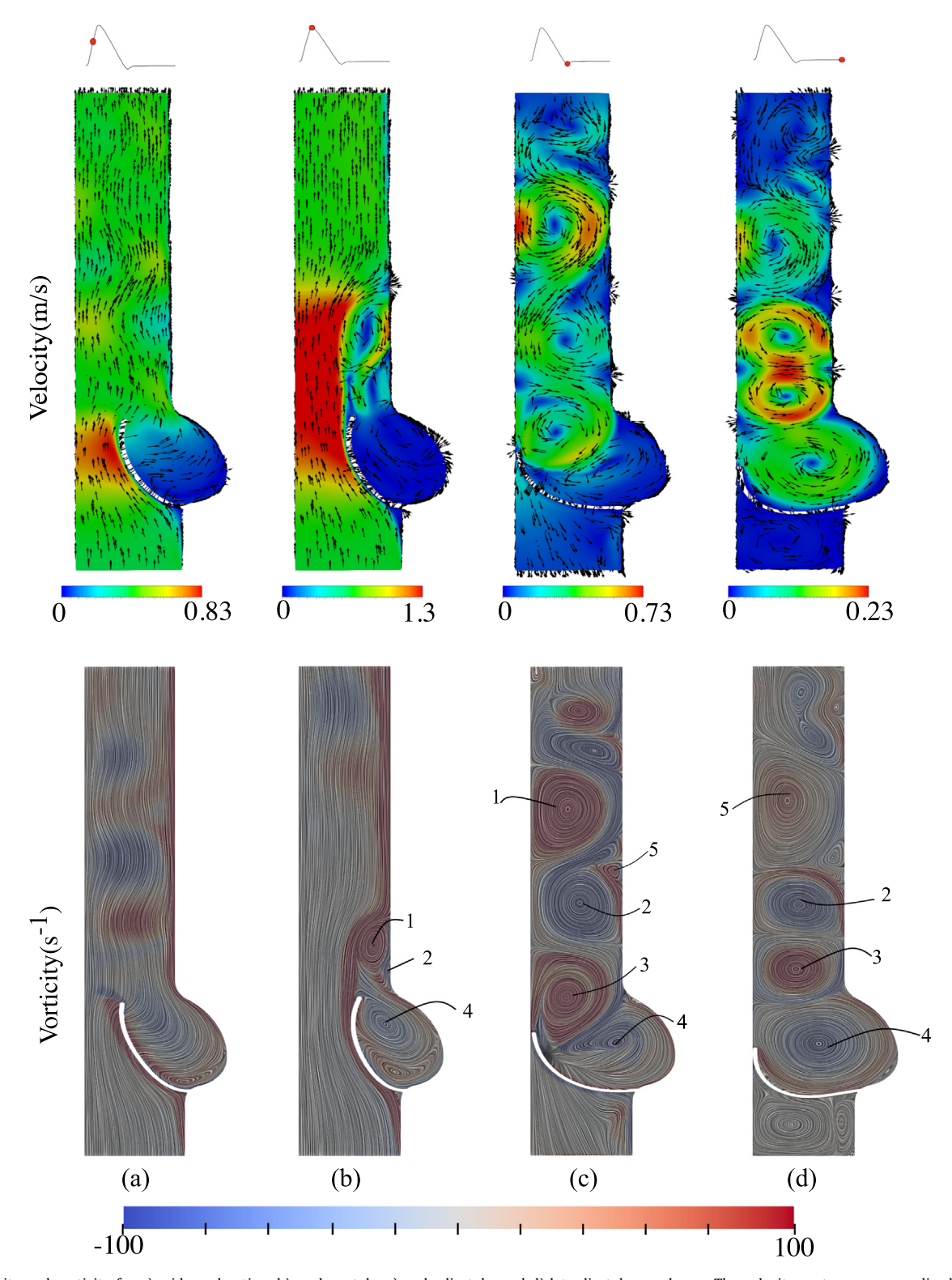


Fig. 2. Velocity and vorticity for a) mid acceleration, b) peak systole, c) early diastole, and d) late diastole are shown. The velocity vectors are normalized. The velocity streamlines are visualized on top of vorticity using surface line integral convolution. The prominent vortex structures are numbered.

## 2.2. Continuum transport

The transport models were based on continuum advection–diffusion equations and were coupled (one-way) with the velocity from the FSI model. The advection–diffusion equation could be written in the ALE framework as

$$\frac{\partial c}{\partial t} + (\mathbf{u} - \mathbf{w}) \cdot \nabla c = D \nabla^2 c, \tag{2}$$

where c is biochemical concentration,  ${\bf u}$  is blood flow velocity,  ${\bf w}$  is the moving mesh velocity, and D is biochemical diffusivity set to a value within the range of biochemical diffusivity in blood (Hansen et al., 2019) (D=10<sup>-5</sup>cm<sup>2</sup>/s). Five different transport boundary con-

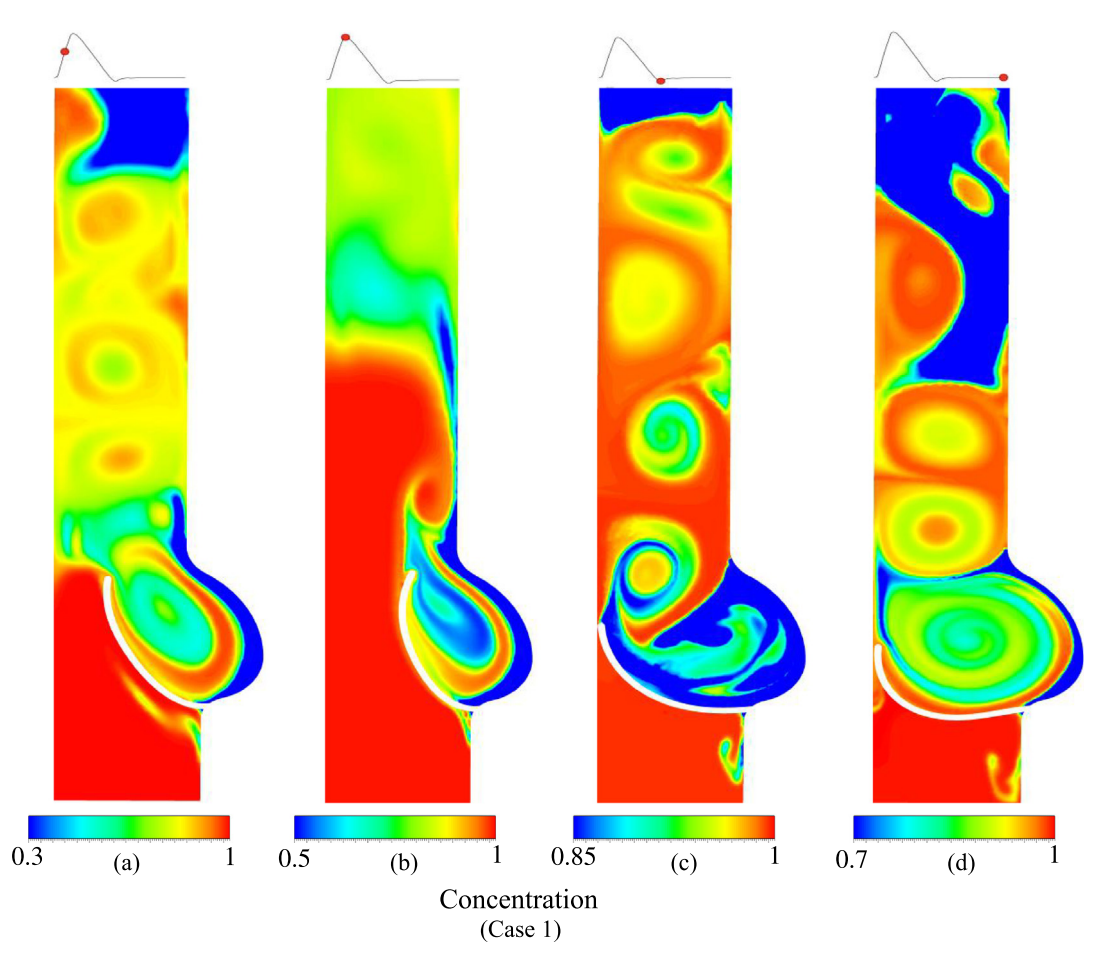


Fig. 3. Case 1 (constant concentration at the inlet) concentration profiles for a) mid acceleration, b) peak systole, c) early diastole, and d) late diastole are shown.

ditions and cases are presented below. Each boundary condition represents a different biotransport process associated with aortic valve disease. The boundary conditions are set to arbitrary values since the goal of this study is to study the connection between qualitative concentration patterns and flow physics. In all cases, zero initial condition is used and zero flux boundary condition is applied at the outlet and aortic wall.

**Case 1.** In this case, constant concentration (c = 1) is prescribed at the inlet. This case represents biochemicals and cells such as platelets that are carried by the blood flow coming out of the heart. Additionally, serum albumin, which can lead to bioprosthetic heart valve degeneration (Frasca et al., 2020) could be studied with this case.

**Case 2.** Constant inward flux is prescribed at the leaflet surface  $(D\frac{\partial c}{\partial n}=1)$  and zero concentration is assumed for the inlet. This scenario models biochemicals produced by the valvular endothelial cells. Monocyte chemoattractant protein-1 (MCP-1) production, which attracts monocytes during calcification initiation (Sridhar et al., 2018) and nitric oxide production, which prevents thrombosis (Loscalzo, 2001) are two examples.

**Case 3.** Case 3 is similar to case 2 but the flux is only applied on the aortic side of the valve (fibrosa). Given the observation that fibrosa is exposed to disturbed hemodynamics (Ge and Sotiropoulos, 2010), this choice models biochemical production by endothelial cells under disturbed flow conditions. For example, it is known that disturbed flow induces atherogenic and thrombogenic biochemical production (Cahill and Redmond, 2016).

Case 4. In this case, constant concentration (c = 1) is applied at the inlet and a Robin boundary condition is applied at the leaflet

surface ( $D\frac{\partial c}{\partial n}$ + pc = 0) where p = 1e-9 cm/s represents endothelial cell permeability to LDL macromolecules. The valvular endothelium permeability to LDL is smaller than the vascular endothelium (Butcher and Nerem, 2007). Herein, the permeability was selected to be an order of magnitude smaller than the vascular permeability reported (Olgac et al., 2008). This case models LDL transport, which is important in calcification.

**Case 5.** Here, residence-time was calculated. The Eulerian residence-time (ERT) model was solved as an advection-diffu sion-reaction equation (Reza and Arzani, 2019)

$$\begin{split} \frac{\partial RT}{\partial t} + \mathbf{u} \cdot \nabla RT &= \nabla \cdot (D \nabla RT) + H(3) \\ H &= \begin{cases} 1 \text{ if } x \in \Gamma \\ 0 \text{ if } x \notin \Gamma \end{cases}, \end{split}$$

where RT is residence-time, and the reaction source term (H) represents time. Zero Dirichlet boundary condition is imposed at the inlet. Seven cardiac cycles are simulated such that ERT results become quasi-steady. Finally, to characterize near-leaflet stagnation, relative residence-time (RRT) was calculated based on wall shear stress (WSS) vectors (Arzani et al., 2017a)

$$RRT = \frac{1}{\|\frac{1}{T} \int_0^T WSS \ dt\|},\tag{4}$$

where T is the cardiac cycle duration.

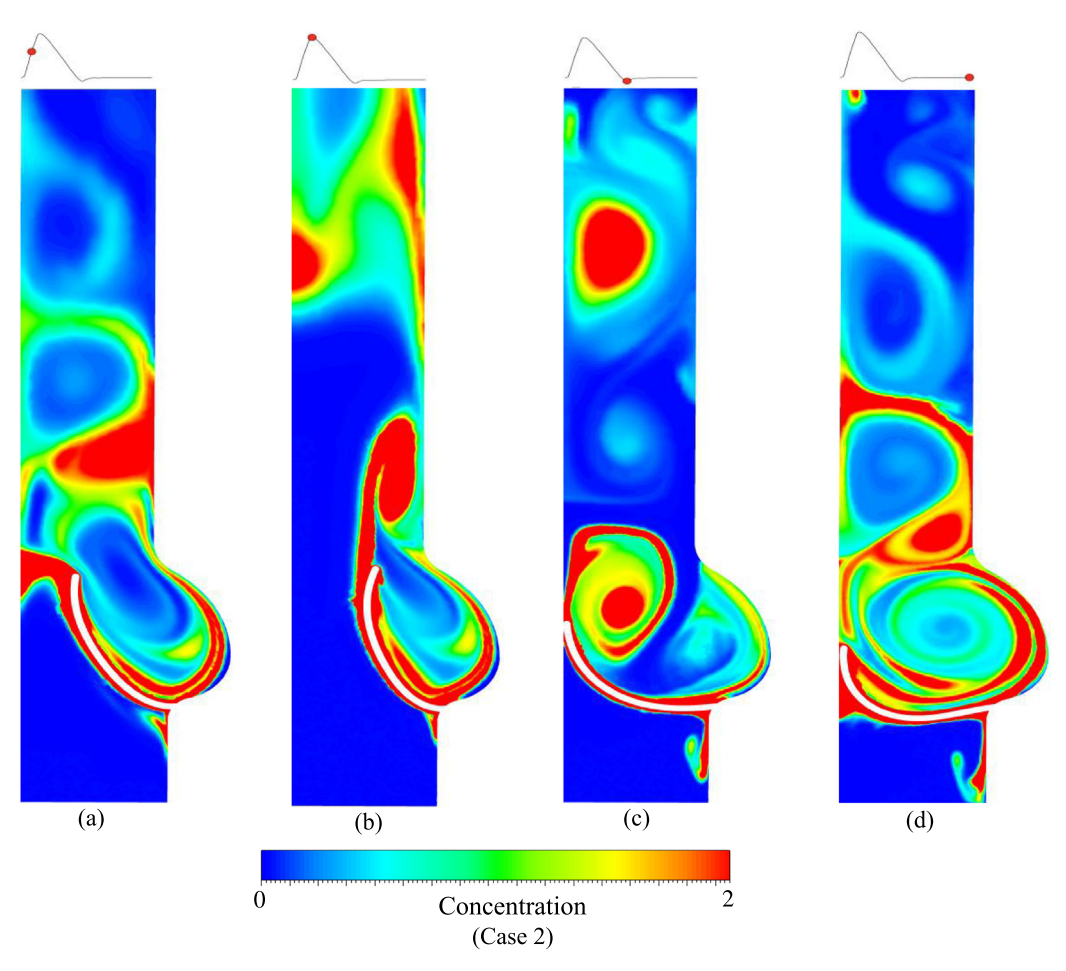


Fig. 4. Case 2 (constant flux at the entire leaflet) concentration profiles for a) mid acceleration, b) peak systole, c) early diastole, and d) late diastole are shown.

#### 2.3. Three-dimensional FSI and transport models

The setup for the 3D model was similar to the mechanical heart valve model used in a recent study (Hedayat et al., 2017). Briefly, the curvilinear immersed boundary (CURVIB) method (Ge and Sotiropoulos, 2007; Asgharzadeh and Borazjani, 2017) is used where a sharp interface is maintained by reconstructing the boundary conditions on the nodes that are adjacent and exterior to the immersed boundary using an interpolation along the local normal to the boundary (Gilmanov and Sotiropoulos, 2005). Platelet activation is calculated for the linear level of activation using an Eulerian frame of reference (Hedayat et al., 2017), in which the advectionreaction equation is discretized using 2nd order muscle scheme and 2nd order total variation diminishing (TVD) Runge-Kutta for spatial and temporal discretization, respectively (Hedayat and Borazjani, 2019). Finally, a continuum transport model is solved for a generic biochemical transport scenario similar to case 1 in 2D where a constant concentration (c = 1) is applied at the inlet. Further details about the 3D models are reported in the Supplementary Materials.

To study the complex flow physics in the 3D model, we computed the Lagrangian coherent structure (LCS) to identify coherent flow structures. LCS is computed by integrating a dense set of Lagrangian tracers and computing the finite-time Lyapunov exponents (FTLE). In this study, backward-in-time integration was performed to detect attracting LCS. Details about LCS calculation are provided elsewhere (Shadden et al., 2010; Arzani and Shadden, 2012).

#### 3. Results

Case 1 to 4 were run for two cardiac cycles, and case 5 (ERT) was run for seven cardiac cycles. The last cardiac cycle of the results is shown. The velocity and vorticity patterns during different intracardiac time-points are shown in Fig. 2. Different vortex structures are generated from the moving leaflet and aortic wall. These vortices are marked in the figure. Vortex 1 is a result of the separation of the shear layer from the ventricular side of the leaflet. The interaction of this vortex with the vessel wall leads to a secondary vortex formation shown as vortex 2. During valve closure, flow separation from the free edge of the leaflet leads to vortex 3. Vortex 4 and 5 are created in the sinus region and from the distal wall, respectively. In the following section, these vortex structures are compared with the concentration patterns.

## 3.1. Mass transport concentration patterns

The concentration patterns during different time-points for case 1 (constant concentration at the inlet) are shown in Fig. 3. Vortex 1 and 2 attract elevated concentration levels in their boundaries and at the same time form transport barriers limiting the concentration level in their vortex core. On the contrary, vortex 3 and 5 attract biochemicals during their formation process and therefore trap higher levels of biochemicals in their core. Vortex 4 remains fairly static in the sinus region and acts as a transport barrier limiting biochemical penetration in its vicinity.

The results for case 2 (constant flux on the entire leaflet) are shown in Fig. 4. In this case, the biochemicals originate from the

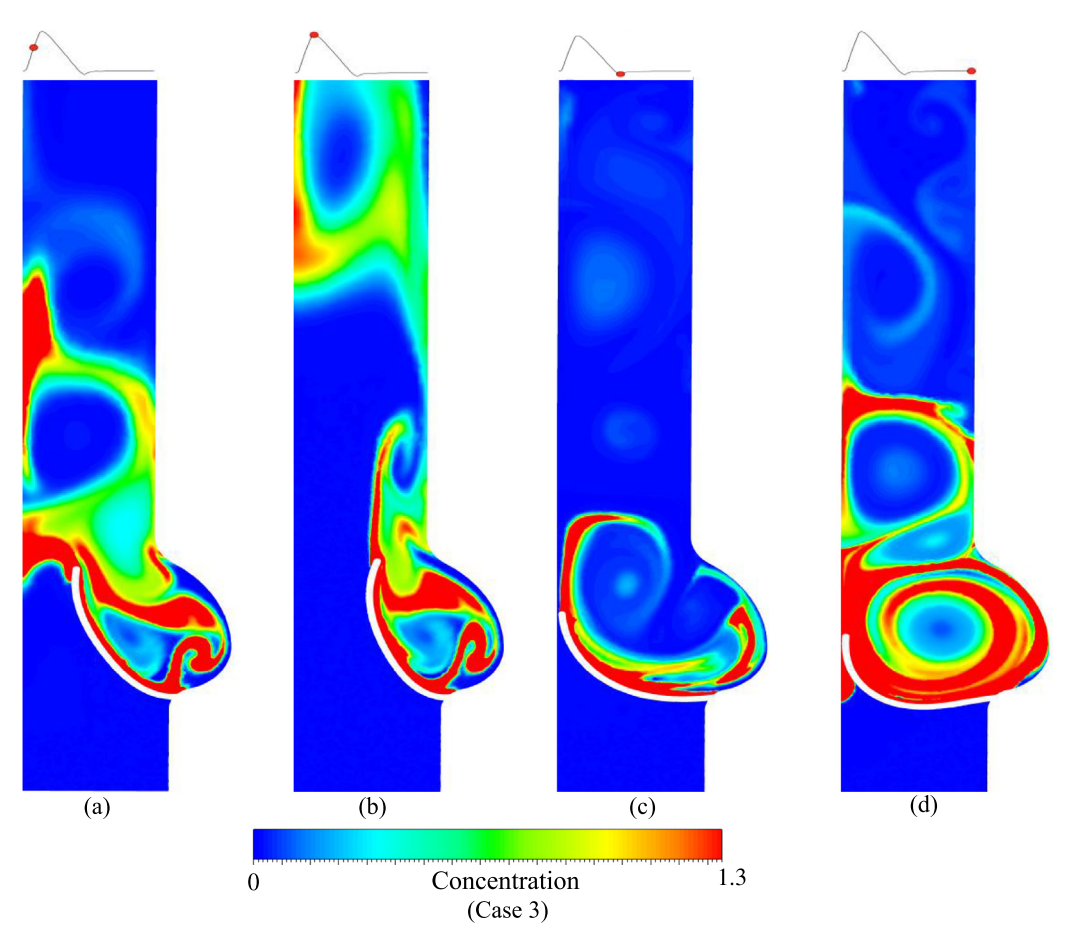


Fig. 5. Case 3 (constant flux at the fibrosa) concentration profiles for a) mid acceleration, b) peak systole, c) early diastole, and d) late diastole are shown.

leaflet, and therefore the vortices that are shed from the leaflet organize their transport. Namely, vortex 1 and 3 attract and carry the biochemicals. Coherent patterns of high concentration could be seen to coincide with these vortices. The other vortices that are generated from the wall form transport barriers and reduced concentration could be seen at the center of those vortices.

Fig. 5 shows the results for case 3. In this case, we are interested in the concentration of biochemicals produced by the aortic side of the valve. In this case, the blood flow emanating from the aortic root and shearing the ventricular side of the leaflet does not carry biochemicals from the leaflet, and therefore reduced biochemical concentration is observed distal to the valve. Vortices such as vortex 1 that are shed from the ventricular side no longer carry high concentration values.

Case 4 (LDL transport) results are shown in Fig. 6. High near-leaflet concentration could be seen due to the concentration polarization effect (Vincent and Weinberg, 2014). During systole, a higher concentration is observed on the ventricular side, and near-leaflet LDL localization at the aortic side occurs during valve closure. The concentration patterns distal to the valve and their relation to vortex structures are similar to case 1.

Finally, the ERT results are shown in Fig. 7. Elevated residencetime is seen on the aortic side of the valve. Particularly, the highest ERT regions localize at the wall of the sinus of Valsalva and the valve attachment region. Vortex 4 that persists in the sinus region leads to elevated flow stagnation in this region. The ERT is relatively low distal to the valve with some local elevated regions corresponding to the vortex structures.

## 3.2. Relationship between WSS and near-leaflet concentration

Herein, we looked into how WSS patterns correlate with near-leaflet transport patterns. We focus on the aortic side (fibrosa) as the region where calcification and thrombosis often occur. The near-leaflet flow patterns and the relationship between TAWSS and leaflet surface concentration are shown in Fig. 8. The positive direction for WSS is assumed to be towards the free edge. To quantify the correlation between WSS and leaflet concentration, two Pearson correlation coefficients are calculated for positive  $(\rho^+)$  and negative  $(\rho^-)$  WSS data as shown in the figure (p < 0.001). The velocity and vorticity patterns near the leaflet are shown in Fig. 8, which influence the WSS patterns. Case 1 (constant concentration at the inlet), case 4 (LDL transport), and case 5 (ERT) are shown in the figure. In case 1, high concentration occurs in the impingement region with the highest concentration at zero TAWSS magnitude. Additionally, the positive TAWSS region that is closer to the leaflet free edge carries higher concentration. In case 4, low concentration is seen at the free edge where positive WSS exists. Elevated concentration is seen in the negative WSS region where the near-wall flow is towards the attachment region. Finally, in case 5, the highest ERT happens at the valve attachment region where the velocity is lower. A relatively strong positive correlation is seen between RRT (a WSS-based measure of near-wall stagnation) and ERT on the leaflet surface. The data for case 2 and 3 are not shown as no correlation between WSS and the concentration results could be observed.

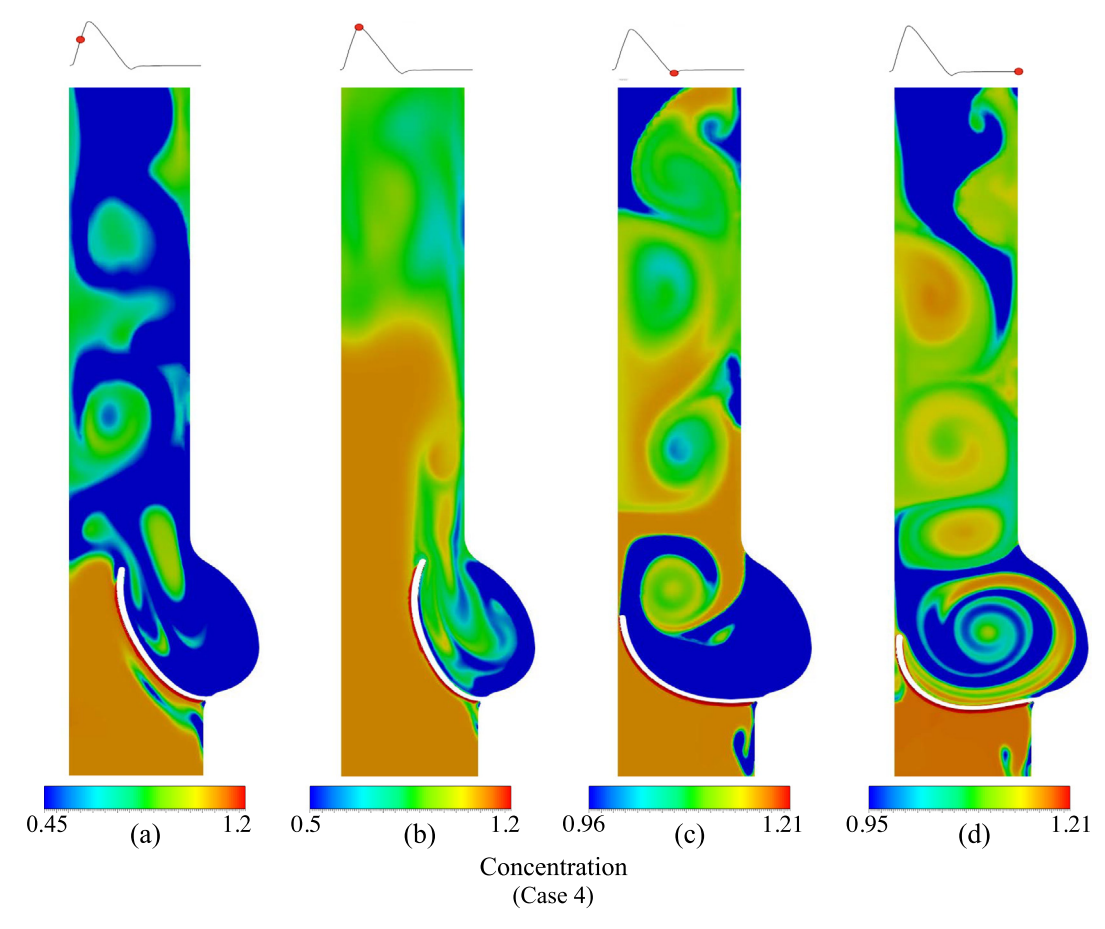


Fig. 6. Case 4 (LDL transport) concentration profiles for a) mid acceleration, b) peak systole, c) early diastole, and d) late diastole are shown.

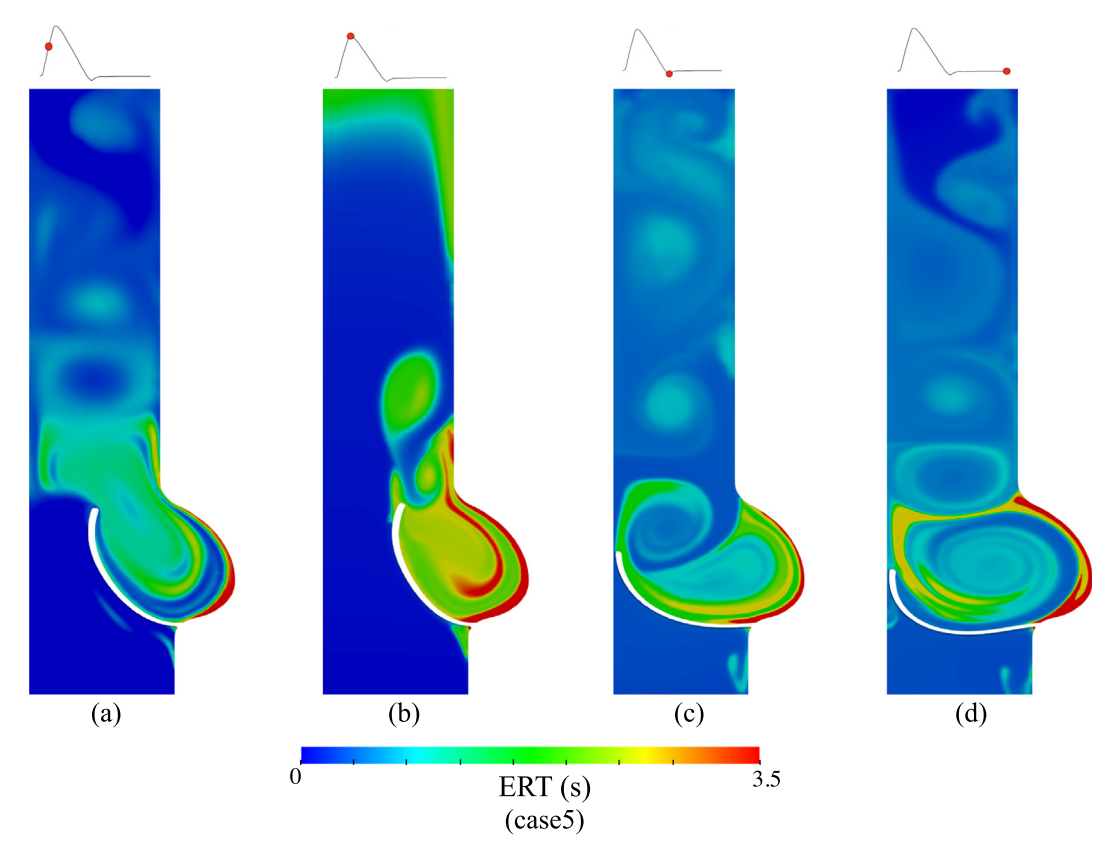
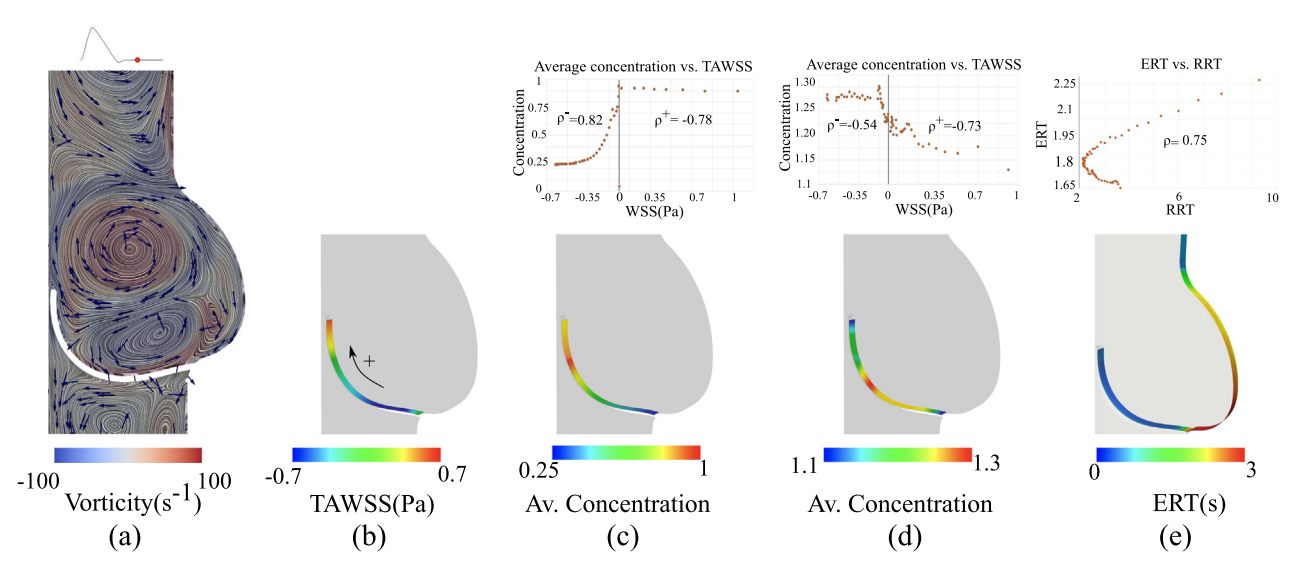


Fig. 7. Case 5 (Eulerian residence-time) results for a) mid acceleration, b) peak systole, c) early diastole, and d) late diastole are shown.



**Fig. 8.** Vorticity contour with normalized velocity vectors during mid diastole (a), time-average WSS (TAWSS) magnitude (b), time-average leaflet concentration contour plot and scatter plot of TAWSS vs. concentration data for case 1 (c) and case 4 (d) are shown. The Pearson correlation coefficients are shown for positive  $(\rho^+, p < 0.001)$  and negative  $(\rho^-, p < 0.001)$  WSS data. Relative residence-time (RRT) vs. Eulerian residence-time (ERT) data are shown in (e). Positive WSS is defined towards the leaflet free edge. In the leaflet attachment region of case 4, a zero-concentration point exists that is not shown in the scatter plot due to the range.

#### 3.3. Three-dimensional mechanical heart valve results

The 3D mechanical heart valve results are shown in Figs. 9 and 10. In Fig. 9, the 3D streamlines are displayed and platelet activation, biochemical concentration, and FTLE results are shown in the three cross-sectional planes. In the top row (red plane containing the valve), it is seen that the high platelet activation results closely follow the LCS (red lines in the FTLE field). A similar observation is made for the concentration results where biochemical concentration patterns are dictated by the LCS. The correspondence between the FTLE and transport results is visible in the two boxes shown in the figure where prominent LCS patterns could be distinguished due to the nature of the flow. In the middle row (blue plane), the LCS forms a clear transport barrier in the proximal region separating the transport results into different regions. Inside this LCS, a coherent jet is identified with low FTLE values, which contains very low platelet activation level and high biochemical concentration. The high platelet activation regions coincide with high FTLE zones where dense LCS structures are present. The final row (transverse plane) clearly shows that these patterns persist in three dimensions. In Fig. 10, two cross-sectional planes and four time-steps of biochemical concentration and FTLE results are shown. A close correspondence between the LCS and concentration patterns could be observed during all time-steps where the LCS either trap biochemicals inside them or prevent biochemical penetration inside the core of the vortex structures.

## 4. Discussion

Despite numerous studies on hemodynamics and flow physics of aortic valve disease, their connection to biochemical transport processes has not received much attention. In this manuscript, we presented various biotransport models that are relevant to calcification and thrombosis and studied their connection with the flow physics and coherent structures. A strong connection was revealed between biotransport and coherent structures identified using vorticity and LCS.

Our results show that the vortices that are trapped in the sinus region (herein, vortex 4) play an important role in enhancing the near-leaflet accumulation and stagnation of biochemicals on the

aortic side of the valve (fibrosa). Fibrosa is of interest clinically because calcification (Yip and Simmons, 2011) and thrombosis (Trusty et al., 2019) are more likely to occur in this region. However, our results also show that under certain transport pathways where biochemicals are originated from the inlet (cases 1 and 4), relatively higher near-leaflet localization occurs on the ventricular side, and near-leaflet localization for fibrosa mostly occurs during the diastole phase. Nevertheless, leaflet-originated biochemical concentration and residence-time are higher on the fibrosa side. We should note that for LDL transport (case 4) we assumed constant permeability. More recent LDL transport models assume WSS-dependent permeability (Alimohammadi et al., 2017) where higher flux occurs in low WSS regions, which could lead to leaflet concentrations in fibrosa that are higher than what we reported.

The complex aortic valve fluid dynamics environment generates different vortex structures from the leaflet and the aortic wall. Depending on the biochemical source (leaflet vs. inlet) and the source of the vortex, each vortex could generate different concentration patterns. This should not be surprising if we recall the vorticity transport equation (Panton, 2013). In 2D flows, the vortex tilting/stretching term vanishes, and therefore the vorticity transport equation reduces to an advection-diffusion equation. The differences with the biochemical transport models are in the boundary conditions and the fact that vorticity can take negative values. This leads to a close correspondence between coherent structures and the concentration patterns. Interestingly, we were able to confirm similar results in 3D where the coherent structures are more complicated. We used FTLE and LCS to identify 3D coherent flow patterns and confirmed our observation in 2D. Our FSI mesh was coarsened distal to the valve, and therefore the 3D continuum transport results were diffused in that region. However, the FTLE field from the Lagrangian discrete approach was still capable of capturing the fine-scale flow features (the upper red box in Fig. 9). Case 1 in the 2D model and the biochemical concentration results in 3D were based on similar boundary conditions and therefore may be compared (Fig. 3 and Fig. 10). It can be seen that the vortices generated in both cases, do not let the biochemicals leave or enter into their domains. That is, a barrier is formed between the core of the vortex and the region outside of the vortex. These vortical structures in both cases determined the biochemical transport patterns.

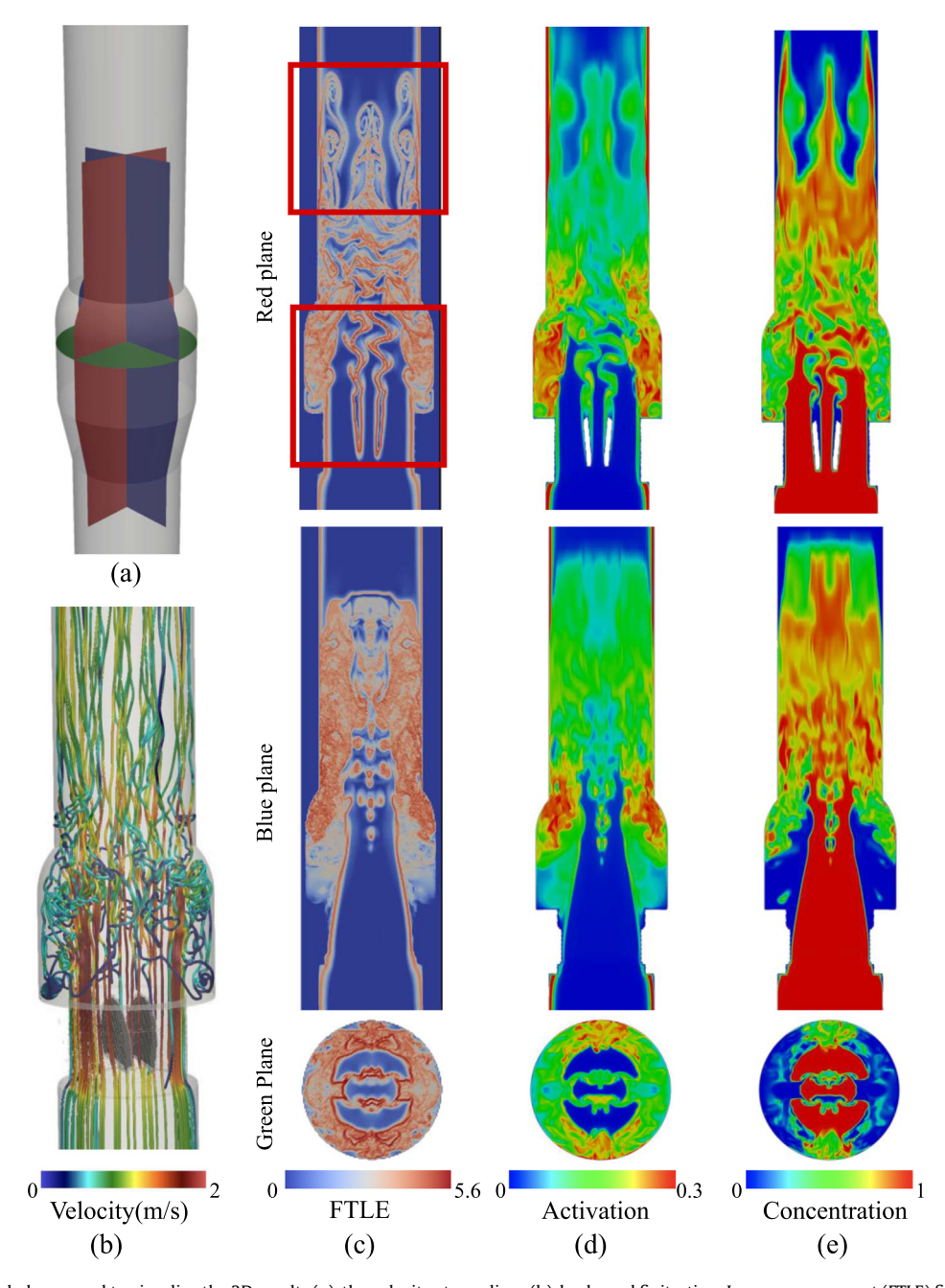


**Fig. 9.** The cross-sectional planes used to visualize the 3D results (a), the velocity streamlines (b), backward finite-time Lyapunov exponent (FTLE) field (c), platelet activation level (d), and biochemical concentration results (e) for the 3D mechanical heart valve simulations are shown at peak systole. The red boxed zones in the FTLE panel highlight the regions where the correspondence between FTLE and transport results is seen.

We also used WSS vectors to study near-leaflet concentration. WSS patterns in cardiovascular flows are closely related to vortex-wall (herein, vortex-leaflet) interaction (Arzani and Shadden, 2018). We observed that leaflet concentrations depended on the sign of WSS vectors (near-leaflet velocity direction) and WSS magnitude. These results confirm our prior rigid arterial flow studies where WSS vector topology controlled near-wall transport patterns (Arzani et al., 2016; Arzani et al., 2017a). Interestingly, our results showed higher leaflet concentration for case 1 at the tip of the valve, which conforms with microfluidic deep vein thrombosis models where particles accumulated at the tip of symmetric valves (Schofield et al., 2020). Additionally, we observed that the attachment region of fibrosa has the highest residence-time. Interestingly, recent clinical data show that thrombus formation could

occur in the attachment region of transcatheter aortic valves (Trusty et al., 2019). Traditionally, WSS is interpreted as the shear stress exerted on valvular endothelial cells. Aortic valve FSI studies often report WSS, however, this has been criticized since valvular endothelial cells and vascular endothelial cells do not exhibit the same response to WSS (Butcher et al., 2004). Our results show that leaflet WSS could potentially be important in aortic valve disease by influencing near-leaflet transport.

Our work has important clinical implications. First, our framework could be used to quantify near-leaflet biochemical localization and stagnation for bioprosthetic or post-TAVR leaflets to assess the risk of thrombosis and inflammation/calcification. Such in silico models could be used to optimize TAVR design and reduce post-operative complications. Our results show that coherent

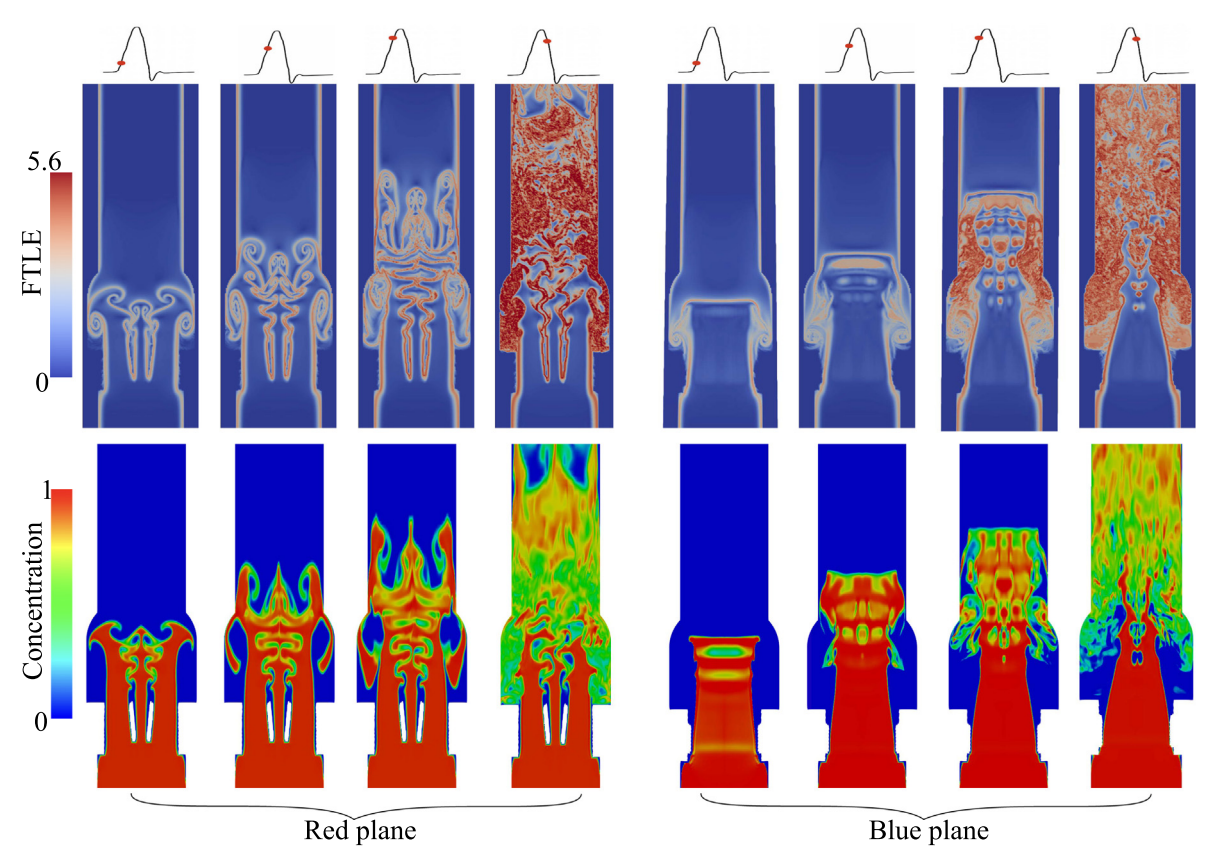


Fig. 10. Biochemical concentration and backward finite-time Lyapunov exponent (FTLE) results for two different cross-sectional planes and during different time-steps are shown for the 3D model. The red and blue planes are marked in Fig. 9.

structures not only control residence-time distribution but also platelet activation patterns. Future studies could exploit these flow physics features to improve designs that reduce thrombosis, which is a major issue with the current TAVR technology (Abdel-Wahab et al., 2018). Finally, our transport models could be extended to develop multiphysics models of thrombus growth.

#### 5. Conclusion

We developed FSI models of generic biotransport processes that represent the blood flow-mediated biochemical pathways in calcification and thrombosis. Our results show that there is a close connection between WSS, vortex structures, and concentration patterns near and distal to the leaflets. This study could be used as a first step towards designing new heart valve replacement technologies that leverage coherent structures to reduce the risk of valve degeneration due to disturbed blood flow.

## **Declaration of Competing Interest**

None.

## Acknowledgement

A. A. acknowledges support from NSF OAC Grant No. 1947559.

#### Appendix A. Supplementary material

Supplementary data associated with this article can be found, in the online version, at https://doi.org/10.1016/j.jbiomech.2021. 110239.

#### References

Abdel-Wahab, M., Simonato, M., Latib, A., Goleski, P.J., et al., 2018. Clinical valve thrombosis after transcatheter aortic valve-in-valve implantation. Circulat.: Cardiovasc. Intervent. 11 (11), e006730.

Alimohammadi, M., Pichardo-Almarza, C., Agu, O., Díaz-Zuccarini, V., 2017. A multiscale modelling approach to understand atherosclerosis formation: A patient-specific case study in the aortic bifurcation. Proc. Inst. Mech. Eng., Part H: J. Eng. Med. 231 (5), 378–390.

Arzani, A., Gambaruto, A.M., Chen, G., Shadden, S.C., 2016. Lagrangian wall shear stress structures and near-wall transport in high-schmidt-number aneurysmal flows. J. Fluid Mech. 790, 158–179.

Arzani, A., Gambaruto, A.M., Chen, G., Shadden, S.C., 2017a. Wall shear stress exposure time: a Lagrangian measure of near-wall stagnation and concentration in cardiovascular flows. Biomech. Model. Mechanobiol. 16 (3), 787–803.

Arzani, A., Masters, K.S., Mofrad, M.R.K., 2017b. Multiscale systems biology model of calcific aortic valve disease progression. ACS Biomater. Sci. Eng. 3 (11), 2922–2033

Arzani, A., Mofrad, M.R.K., 2017. A strain-based finite element model for calcification progression in aortic valves. J. Biomech. 65, 216–220.

Arzani, A., Shadden, S.C., 2012. Characterization of the transport topology in patient-specific abdominal aortic aneurysm models. Phys. Fluids (1994present) 24 (8), 081901.

Arzani, A., Shadden, S.C., 2018. Wall shear stress fixed points in cardiovascular fluid mechanics. J. Biomech. 73, 145–152.

Asgharzadeh, H., Borazjani, I., 2017. A Newton-Krylov method with an approximate analytical Jacobian for implicit solution of Navier-Stokes equations on staggered overset-curvilinear grids with immersed boundaries. J. Comput. Phys. 331, 227–256.

- Borazjani, I., 2013. Fluid-structure interaction, immersed boundary-finite element method simulations of bio-prosthetic heart valves. Comput. Methods Appl. Mech. Eng. 257, 103–116.
- Buendía, P., Montes de Oca, A., Madueño, J.A., Merino, A., Martín-Malo, A., Aljama, P., Ramírez, R., Rodríguez, M., Carracedo, J., 2015. Endothelial microparticles mediate inflammation-induced vascular calcification. FASEB J. 29 (1), 173–181.
- Butcher, J.T., Nerem, R.M., 2007. Valvular endothelial cells and the mechanoregulation of valvular pathology. Philosoph. Trans. Roy. Soc. B: Biolog. Sci. 362 (1484), 1445–1457.
- Butcher, J.T., Penrod, A.M., García, A.J., Nerem, R.M., 2004. Unique morphology and focal adhesion development of valvular endothelial cells in static and fluid flow environments. Arterioscler. Thromb. Vasc. Biol. 24 (8), 1429–1434.
- Cahill, P.A., Redmond, E.M., 2016. Vascular endothelium–gatekeeper of vessel health. Atherosclerosis 248, 97–109.
- Cao, K., Sucosky, P., 2017. Computational comparison of regional stress and deformation characteristics in tricuspid and bicuspid aortic valve leaflets. Int. J. Num. Methods Biomed. Eng. 33 (3), e02798.
- Chen, J.H., Simmons, C.A., 2011. Cell–matrix interactions in the pathobiology of calcific aortic valve disease critical roles for matricellular, matricrine, and matrix mechanics cues. Circ. Res. 108 (12), 1510–1524.
- Chen, Y., Luo, H., 2020. Pressure distribution over the leaflets and effect of bending stiffness on fluid-structure interaction of the aortic valve. J. Fluid Mech. 883, A52.
- Cito, S., Mazzeo, M.D., Badimon, L., 2013. A review of macroscopic thrombus modeling methods. Thromb. Res. 131 (2), 116–124.
- De Marchena, E., Mesa, J., Pomenti, S., et al., 2015. Thrombus formation following transcatheter aortic valve replacement. JACC: Cardiovasc. Intervent. 8 (5), 728–739.
- Frasca, A., Xue, Y., Kossar, A.P., Keeney, S., et al., 2020. Glycation and serum albumin infiltration contribute to the structural degeneration of bioprosthetic heart valves. bioRxiv.
- Ge, L., Sotiropoulos, F., 2007. A numerical method for solving the 3D unsteady incompressible Navier-Stokes equations in curvilinear domains with complex immersed boundaries. J. Comput. Phys. 225 (2), 1782–1809.
- Ge, L., Sotiropoulos, F., 2010. Direction and magnitude of blood flow shear stresses on the leaflets of aortic valves: is there a link with valve calcification?. J. Biomech. Eng. 132 (1), 014505.
- Ghosh, R.P., Marom, G., Bianchi, M., D'souza, K., Zietak, W., Bluestein, D., 2020. Numerical evaluation of transcatheter aortic valve performance during heart beating and its post-deployment fluid-structure interaction analysis. Biomech. Model. Mechanobiol., 1–16
- Gilmanov, A., Barker, A., Stolarski, H., Sotiropoulos, F., 2019. Image-guided fluidstructure interaction simulation of transvalvular hemodynamics: Quantifying the effects of varying aortic valve leaflet thickness. Fluids 4 (3), 119.
- Gilmanov, A., Sotiropoulos, F., 2005. A hybrid cartesian/immersed boundary method for simulating flows with 3D, geometrically complex, moving bodies. J. Comput. Phys. 207 (2), 457–492.
- Hansen, K.B., Arzani, A., Shadden, S.C., 2019. Finite element modeling of near-wall mass transport in cardiovascular flows. Int. J. Num. Methods Biomed. Eng. 35 (1), e3148.
- Hedayat, M., Asgharzadeh, H., Borazjani, I., 2017. Platelet activation of mechanical versus bioprosthetic heart valves during systole. J. Biomech. 56, 111–116.
- Hedayat, M., Borazjani, I., 2019. Comparison of platelet activation through hinge vs bulk flow in bileaflet mechanical heart valves. J. Biomech. 83, 280–290.
- Joda, A., Jin, Z., Summers, J., Korossis, S., 2019. Comparison of a fixed-grid and arbitrary lagrangian-eulerian methods on modelling fluid-structure interaction of the aortic valve. Proc. Inst. Mech. Eng., Part H: J. Eng. Med. 233 (5), 544–553.
- Kamensky, D., Hsu, M.C., Schillinger, D., Evans, J.A., Aggarwal, A., Bazilevs, Y., Sacks, M.S., Hughes, T.J.R., 2015. An immersogeometric variational framework for fluid-structure interaction: Application to bioprosthetic heart valves. Comput. Methods Appl. Mech. Eng. 284, 1005–1053.
- Kandail, H.S., Trivedi, S.D., Shaikh, A.C., Bajwa, T.K., O'Hair, D.P., Jahangir, A., LaDisa Jr, J.F., 2018. Impact of annular and supra-annular CoreValve deployment locations on aortic and coronary artery hemodynamics. J. Mech. Behav. Biomed. Mater. 86, 131–142.
- Korossis, S.A., Booth, C., Wilcox, H.E., Watterson, K.G., Kearney, J.N., Fisher, J., Ingham, E., 2002. Tissue engineering of cardiac valve prostheses II: biomechanical characterization of decellularized porcine aortic heart valves. J. Heart Valve Dis. 11 (4), 463–471.

- Kulik, A., Rubens, F.D., Wells, P.S., Kearon, C., Mesana, T.G., van Berkom, J., Lam, B., 2006. Early postoperative anticoagulation after mechanical valve replacement: a systematic review. Ann. Thoracic Surg. 81 (2), 770–781.
- Leiderman, K., Fogelson, A.L., 2011. Grow with the flow: a spatial-temporal model of platelet deposition and blood coagulation under flow. Mathem. Med. Biol. 28 (1), 47–84.
- Loscalzo, J., 2001. Nitric oxide insufficiency, platelet activation, and arterial thrombosis. Circ. Res. 88 (8), 756–762.
- Lowe, G.D.O., 2003. Virchow's triad revisited: abnormal flow. Pathophysiol. Haemost. Thromb. 33 (5–6), 455–457.
- Makkar, R.R., Fontana, G., Jilaihawi, H., Chakravarty, T., Kofoed, K.F., et al., 2015. Possible subclinical leaflet thrombosis in bioprosthetic aortic valves. N. Engl. J. Med. 373 (21), 2015–2024.
- Midha, P.A., Raghav, V., Sharma, R., Condado, J.F., Okafor, I.U., Rami, T., Kumar, G., Thourani, V.H., Jilaihawi, H., Babaliaros, V., Makkar, R.R., P., Y.A., 2017. The fluid mechanics of transcatheter heart valve leaflet thrombosis in the neosinus. Circulation 136 (17), 1598–1609.
- Morbiducci, U., Ponzini, R., Nobili, M., Massai, D., Montevecchi, F.M., Bluestein, D., Redaelli, A., 2009. Blood damage safety of prosthetic heart valves. shearinduced platelet activation and local flow dynamics: A fluid-structure interaction approach. J. Biomech. 42 (12), 1952–1960.
- Olgac, U., Kurtcuoglu, V., Poulikakos, D., 2008. Computational modeling of coupled blood-wall mass transport of LDL: effects of local wall shear stress. Am. J. Physiol.-Heart Circul. Physiol. 294 (2), H909–H919.
- Panton, R.L., 2013. Incompressible Flow. John Wiley & Sons.
- Pawade, T.A., Newby, D.E., Dweck, M.R., 2015. Calcification in aortic stenosis: the skeleton key. J. Am. Coll. Cardiol. 66 (5), 561–577.
- Raghav, V., Clifford, C., Midha, P., Okafor, I., Thurow, B., Yoganathan, A.P., 2019. Three-dimensional extent of flow stagnation in transcatheter heart valves. J. Roy. Soc. Interf. 16 (154), 20190063.
- Reza, M.M.S., Arzani, A., 2019. A critical comparison of different residence time measures in aneurysms. J. Biomech. 88, 122–129.
- Schofield, Z., Baksamawi, H.A., Campos, J., Alexiadis, A., Nash, G.B., Brill, A., Vigolo, D., 2020. The role of valve stiffness in the insurgence of deep vein thrombosis. Commun. Mater. 1 (1), 1–10.
- Shadden, S.C., Astorino, M., Gerbeau, J.F., 2010. Computational analysis of an aortic valve jet with Lagrangian coherent structures. Chaos: An Interdisciplinary. J. Nonlinear Sci. 20 (1), 017512.
- Sridhar, S., Pham, D.H., Gee, T.W., Hua, J., Butcher, J.T., 2018. Monocytes and macrophages in heart valves: Uninvited guests or critical performers?. Current Opin. Biomed. Eng. 5, 82–89.
- Trusty, P.M., Sadri, V., Madukauwa-David, I.D., Funnell, E., Kamioka, N., Sharma, R., Makkar, R., Babaliaros, V., Yoganathan, A.P., 2019. Neosinus flow stasis correlates with thrombus volume post-TAVR: a patient-specific in vitro study. JACC: Cardiovasc. Intervent. 12 (13), 1288–1290.
- Vahidkhah, K., Azadani, A.N., 2017. Supra-annular valve-in-valve implantation reduces blood stasis on the transcatheter aortic valve leaflets. J. Biomech. 58, 114–122.
- Vincent, P.E., Weinberg, P.D., 2014. Flow-dependent concentration polarization and the endothelial glycocalyx layer: multi-scale aspects of arterial mass transport and their implications for atherosclerosis. Biomech. Model. Mechanobiol. 13 (2), 313–326.
- Weinberg, E.J., Mack, P.J., Schoen, F.J., García-Cardeña, G., Mofrad, M.R.K., 2010. Hemodynamic environments from opposing sides of human aortic valve leaflets evoke distinct endothelial phenotypes in vitro. Cardiovasc. Eng. 10 (1), 5–11.
- Weinberg, E.J., Mofrad, M.R.K., 2007. Transient, three-dimensional, multiscale simulations of the human aortic valve. Cardiovasc. Eng. 7 (4), 140–155.
- Weinberg, E.J., Mofrad, M.R.K., 2008. A multiscale computational comparison of the bicuspid and tricuspid aortic valves in relation to calcific aortic stenosis. J. Biomech. 41 (16), 3482–3487.
- Xenos, M., Girdhar, G., Alemu, Y., Jesty, J., Slepian, M., Einav, S., Bluestein, D., 2010. Device thrombogenicity emulator (DTE)- design optimization methodology for cardiovascular devices: A study in two bileaflet MHV designs. J. Biomech. 43 (12), 2400–2409.
- Yip, C.Y.Y., Simmons, C.A., 2011. The aortic valve microenvironment and its role in calcific aortic valve disease. Cardiovasc. Pathol. 20 (3), 177–182.
- Zakaria, M.S., Ismail, F., Tamagawa, M., Aziz, A.F.A., Wiriadidjaja, S., Basri, A.A., Ahmad, K.A., 2017. Review of numerical methods for simulation of mechanical heart valves and the potential for blood clotting. Med. Biolog. Eng. Comput. 55 (9), 1519–1548.